IEEE Access
Multidisciplinary ⋮ Rapid Review ⋮ Open Access Journal

Received October 10, 2020, accepted November 1, 2020, date of publication November 25, 2020,
date of current version December 17, 2020.

Digital Object Identifier 10.1109/ACCESS.2020.3039281

Blind Image Deblurring via Local Maximum Difference Prior

JING LIU[1], JIEQING TAN[1], LEI HE[2], XIANYU GE[1], (Student Member, IEEE), AND DANDAN HU[2]
[1]School of Computer and Information, Hefei University of Technology, Hefei 230009, China
[2]School of Mathematics, Hefei University of Technology, Hefei 230009, China

Corresponding author: Jieqing Tan (jieqingtan@hfut.edu.cn)

This work was supported by the National Natural Science Foundation of China under Grant 61472466.

ABSTRACT Blind image deblurring is a well-known conundrum in the digital image processing field. To get a solid and pleasing deblurred result, reasonable statistical prior of the true image and the blur kernel is required. In this work, a novel and efficient blind image deblurring method which utilizes the Local Maximum Difference Prior (*LMD*) is presented. We find that the maximum value of the sum of the differences between the intensity of one pixel and its surrounding 8 pixels in the local image patch becomes smaller with motion blur. This phenomenon is an intrinsic feature of the motion blur process, we demonstrate it theoretically in this paper. By introducing a linear operator to compute *LMD* and adopting the L_1 norm constrain to the *LMD* involved term, an effective optimization scheme which makes use of a half-quadratic splitting strategy is exploited. Experimental results show that the presented method is more robust and outperforms the most advanced deblurring methods on both composite images and ground-truth scenes. Besides, this algorithm is more general because it does not require any heuristic edge selection steps or need too many extreme value pixels in the input image.

INDEX TERMS Image deblurring, image restoration, deconvolution, kernel estimation, local maximum difference.

I. INTRODUCTION

The task of image deblurring is to obtain a clear image from a blurred measurement, which is a hot and famous topic [2] in the computer vision and image processing domain. If the blur kernel is shift-invariant, the blurred observation B can be expressed as the convolution of the underlying true scene I and a blur kernel k:

$$B = I \otimes k + n \tag{1}$$

where $\otimes$ is the convolution symbol, n is unavoidable random noise. When the blur kernel k is unknown, it becomes a classical ill-conditioned problem to obtain a clear image from the model (1). There are countless groups of I and k getting the identical B, e.g., a trivial solution: blurred measurement itself and delta kernel.

To solve this problem, additional constraints and prior knowledge are required. In a general way, most existing methods take advantage of statistical priors of blur kernels and latent images [3], [5], [14], [22], [29], [31], [35], [36], [41], [46], or edge-prediction strategies [8], [10], [11], [23]. Nevertheless, the edge-based methods will fail when there are no available strong edges. Therefore, prior-based methods have captured considerable attention in recent years. Among them are heavy-tailed distribution of the gradient [5], L_1/L_2 prior [14], L_0 gradient [22], patch-based prior [29], color-line prior [31], dark channel prior [35], low-rank prior [36], extreme channel prior [41] and local maximum gradient prior [46], just to name a few. Although these methods perform well, there is still room for improvement.

In this paper, we put forward a blind image deblurring algorithm via a novel natural image prior (*LMD*). We find an interesting phenomenon: the maximum value of the sum of the differences between the intensity of one pixel and its surrounding 8 pixels in the local image patch will decrease with the blurring process. We testify it mathematically. By enforcing the L_1 norm constrain to the *LMD* involved term and the L_0 norm constrain to the gradient involved term, we present a valid optimization scheme. The half-quadratic splitting method is employed to handle this non-convex minimum problem [16]. Extensive experimental results indicate that our

The associate editor coordinating the review of this manuscript and approving it for publication was Shiqi Wang.

algorithm performs well on both natural images and special scenario images. For instance, text [4], [17], [18], [26], [32], face [25], [48], low-light images [27].

The main contributions of this work are as follows: we present a new image prior called *LMD*, prove that the values of *LMD* decrease with the blurring process, and introduce a linear operator to compute *LMD*. Our approach performs favorably on both composite images [9], [19], [26], [34] and ground-truth images [34] against the most advanced approaches.

II. RELATED WORK

For the past few years, image deblurring technology has aroused broad attention because of its practical applications. The most advanced algorithms either utilized prior knowledge or detected useful edges for kernel estimation [8], [10], [11], [23]. In this section, we introduce some literature relating to this article.

Joshi *et al.* [8] presented to use sub-pixel differences precision to extract salient edges from blurry input. In [10], Cho and Lee introduced a scale circulation strategy and made use of the image gradient to reduce the running time. Sun *et al.* [23] adopted a patch prior to refine the method [10], but this algorithm is time-consuming. Xu and Jia [11] discovered that strong edges are not always conducive to kernel estimation. On this basis, they proposed a two-phase method to optimize the kernel estimation process. The edge-based methods mentioned above will encounter an obstacle when there are no available salient edge.

In order to achieve better image deblurring effect, other existing approaches took advantage of prior knowledge [5], [7], [14], [22], [29], [31], [35] and additional information [27], [32], [37] to dispose gradient prior to image deblurring. Shan *et al.* [7] used a unified probabilistic framework to dispose of both non-blind and blind deblurring problems. Krishnan *et al.* [14] proposed a new minimization scheme with normalized sparsity prior. However, this method may miss texture details in motion deblurring. Xu *et al.* [22] developed a new data fidelity term and accelerated the deblurring process. In [29], Michaeli and Ironi made use of patch recurrence prior to realize image deblurring. Lai *et al.* [31] introduced a color-line prior and used it to restore sharp edges. Pan *et al.* [35] utilized dark channel prior to solve the ill-posed problem and achieved favorable performance. Yan *et al.* [41] introduced a bright channel prior to improve Pan's method [35]. The two algorithms mentioned above cannot achieve a satisfying result when the underlying true image has no extreme pixels.

Recently, learning-based methods have been developed to motion deblurring [33], [38]–[40], [42]–[45]. Schuler *et al.* [38] estimated the blur kernel by a deep network and then used a proper non-blind method to estimate the final clear image. Chakrabarti *et al.* [39] learned the Fourier coefficients of a deconvolution filter via a CNN network structure. Yan *et al.* [40] estimated the blur kernel via classification and regression. Nah *et al.* [42] trained a multi-scale CNN which directly yields latent clear images without any explicit blur kernel estimate process. Li *et al.* [45] learned a discriminative prior via a CNN network structure, and then combined it with a traditional framework to fulfill image deblurring task. Nevertheless, when it comes to images with complex and large motion blurs, some of them cannot perform well.

III. MAXIMUM DIFFERENCE PRIOR

In this section, we first describe a fresh statistical prior named *LMD* and then state why it works during the blind image deblurring process. In the end, we show how to solve the *LMD* involved term.

A. THE DEFINITION OF LMD

The local maximum difference(*LMD*) is defined by

$$LMD\left(I\right)\left(x\right)=\max_{c\in\{r,g,b\}}\left(\max_{y\in P(x)}\left(\left|D\left(I^{c}\right)\left(y\right)\right|\right)\right) \tag{2}$$

where x and y denote pixel locations in the image, $P(x)$ is an $n\times n$ local patch and x is its center, c belongs to color channel set $\{r, g, b\}$. The difference value of the pixel location y is simply expressed as

$$\left|D\left(I^{c}\right)\left(y\right)\right|=\sum_{z\in H(y)}\left|I^{c}\left(y\right)-I^{c}\left(z\right)\right| \tag{3}$$

where $H(y)$ represents a 3×3 image patch centered at y, z denotes pixel location in it.

B. THE ANALYSIS OF LMD

To take advantage of *LMD* during deblurring, we analyze how the value of *LMD* varies with motion blur. As shown in Fig. 1, the blurring process reduces the *LMD* value. Thus, maximizing *LMD* value is beneficial to image recovery.

What is more, our observation is confirmed on the PASCAL 2012 dataset [30] by selecting 2000 clean images at random and blurring these images with eight different blur kernels from [9] to obtain 2000 blurry images. We calculate the *LMD* values of those 4000 images, compute the intensity histograms for *LMD* elements of both clear images and blurred images respectively, and compare the average of the *LMD* elements of each pair of the clean image and the corresponding blurred images. Fig. 2 (a) and Fig. 2(b) manifest that most *LMD* values of clean images range from 0 to 8, while the *LMD* values of blurred images are between 0 and 2. Fig. 2 (c) illustrates that the average of the *LMD* elements of a clean image is greater than that of the corresponding blurred image. That is to say, the *LMD* value will diminish after the blurring process. To further verify the above observation, we prove it mathematically.

FIGURE 1. The deblurring results of a natural image. (a) Input, (b) Our result, (c) *LMD* map of (a), (d) *LMD* map of (b).

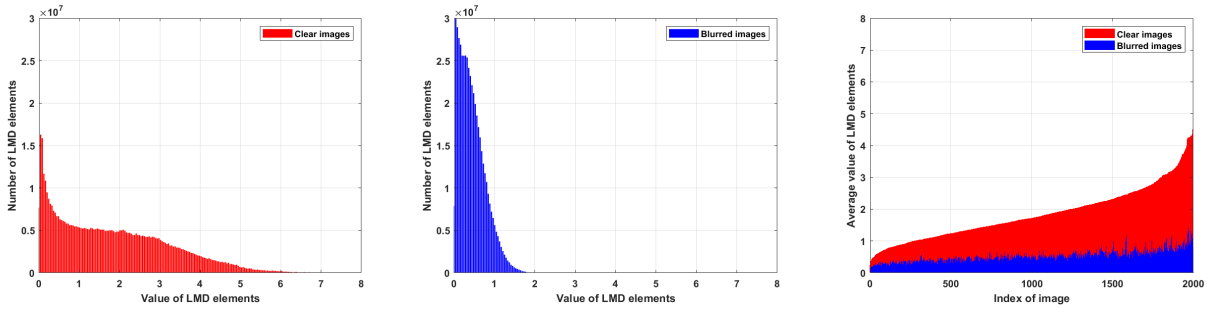

FIGURE 2. The Intensity histograms for *LMD* elements of both clean images and blurred images. (a) Intensity histograms for *LMD* elements of clean images, (b) Intensity histograms for *LMD* elements of blurred images, (c) The average of the *LMD* elements of each pair of clean image and corresponding blurred image.

If B is a gray-scale image, according to the definition of local maximum difference

$$\begin{aligned} LMD\left(B\right)\left(x\right) &= \max_{y\in P(x)} \left|D\left(B\right)\left(y\right)\right| \\ &= \max_{y\in P(x)} \left|\sum_{t\in\Omega_k} D\left(I\right)\left(y+\left[\frac{s}{2}\right]-t\right)k\left(t\right)\right| \\ &\leq \max_{y\in P(x)} \left[\sum_{t\in\Omega_k} \left|D\left(I\right)\left(y+\left[\frac{s}{2}\right]-t\right)\right| k\left(t\right)\right] \\ &\leq \sum_{t\in\Omega_k} \max_{y\in P(x)} \left|D\left(I\right)\left(y+\left[\frac{s}{2}\right]-t\right)\right| k\left(t\right) \\ &\leq \sum_{t\in\Omega_k} \max_{y\in P'(x)} \left|D\left(I\right)\left(y\right)\right| k\left(t\right) \\ &= \max_{y\in P'(x)} \left|D\left(I\right)\left(y\right)\right| \\ &= LMD\left(I\right)\left(x\right) \end{aligned} \tag{4}$$

where Ω_k is the domain of blur kernel k, s is the size of kernel k, $k\left(t\right)\geq 0$, $\sum_{t\in\Omega_k} k\left(t\right)=1$. S_P and $S_{P'}$ are the sizes of local patches $P\left(x\right)$ and $P'\left(x\right)$. We have $S_{P'}=S_P+s$. Eq.(4) is extended by adding the color channels,

$$\begin{aligned} &\max_{c\in\{r,g,b\}} \left(\max_{y\in P(x)} \left(\left|D\left(B^c\right)\left(y\right)\right|\right)\right) \\ &\qquad \leq \max_{c\in\{r,g,b\}} \left(\max_{y\in P(x)} \left(\left|D\left(I^c\right)\left(y\right)\right|\right)\right) \end{aligned} \tag{5}$$

According to the definition of *LMD*, the above equation is equivalent to,

$$LMD\left(B\right)\left(x\right) \leq LMD\left(I\right)\left(x\right) \tag{6}$$

If $I\left(x\right)\in[0,1]$, $LMD\left(I\right)\left(x\right)\in[0,8]$, thus

$$0\leq 8-LMD\left(I\right)\left(x\right)\leq 8-LMD\left(B\right)\left(x\right)\leq 8 \tag{7}$$

Enforcing the L_1-norm [6], [7] to the *LMD* relevant term, we have

$$\left\|8-LMD\left(I\right)\right\|_1 \leq \left\|8-LMD\left(B\right)\right\|_1 \tag{8}$$

Minimizing the term $\left\|8-LMD\left(\cdot\right)\right\|_1$ favors clear image rather than blurred image.

C. THE CALCULATION OF LMD

To build an executable optimization model, we first consider how to calculate the *LMD* operator. The *LMD* is expressed as a linear operator multiplied by the vector form of image $\mathbf{I}$. The *LMD* operator is equal to the product of the difference operator, the absolute value operator, and the local maximum operator. From (3) we know that the difference value of the pixel location (m,n) has eight directions as follows.

$$\begin{aligned} D_1\left(I\right)\left(m,n\right) &= I\left(m,n\right)-I\left(m,n-1\right); \\ D_2\left(I\right)\left(m,n\right) &= I\left(m,n\right)-I\left(m,n+1\right); \\ D_3\left(I\right)\left(m,n\right) &= I\left(m,n\right)-I\left(m-1,n\right); \\ D_4\left(I\right)\left(m,n\right) &= I\left(m,n\right)-I\left(m+1,n\right); \\ D_5\left(I\right)\left(m,n\right) &= I\left(m,n\right)-I\left(m-1,n-1\right); \\ D_6\left(I\right)\left(m,n\right) &= I\left(m,n\right)-I\left(m+1,n+1\right); \end{aligned}$$

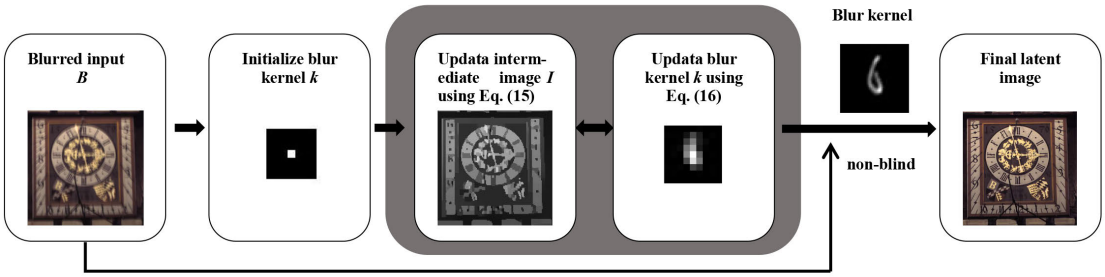

FIGURE 3. The frameworks of the presented algorithm. The gray box denotes the process of blur kernel estimation. After obtaining the estimated blur kernel at the finest layer, we use a proper non-blind deblurring method to restore the final clear image.

$$D_7(I)(m,n) = I(m,n) - I(m+1,n-1);$$
$$D_8(I)(m,n) = I(m,n) - I(m-1,n+1); \quad (9)$$

The difference operator can be written as,

$$\mathbf{D} = (\mathbf{D_1}, \mathbf{D_2}, \cdots \mathbf{D_8})^T \quad (10)$$

The max operator and $|\cdot|$ operator are usually denoted as matrix forms. $|\cdot|$ is equal to a matrix $\mathbf{A}$ multiplied by the vector form of $\mathbf{D}(\mathbf{I})$. The difference value $\mathbf{D}(\mathbf{I})$ has eight directions, so the absolute value operator also has eight directions $\mathbf{A} = (\mathbf{A_1}, \mathbf{A_2}, \cdots \mathbf{A_8})^{\mathbf{T}}$. Suppose the number of dimensions of $\mathbf{D}(\mathbf{I})$ is N, and $\mathbf{A}$ is an $N \times N$ diagonal matrix. In addition, the diagonal elements of $\mathbf{A}$ belong to $\{-1, 1\}$. For example,

$$\mathbf{A_1}(m,m) = \begin{cases} 1, & \mathbf{D_1}(\mathbf{I})(m) \geq 0 \\ -1, & \mathbf{D_1}(\mathbf{I})(m) < 0 \end{cases} \quad (11)$$

Similar for $\mathbf{A_2}, \cdots, \mathbf{A_8}$. The local maximum operator [35] can be viewed as a sparse matrix $\mathbf{M}$, satisfying

$$\mathbf{M}(x,w) = \begin{cases} 1, & w = \arg\max_{y \in P(x)} |\mathbf{D}(\mathbf{I})(y)| \\ 0, & otherwise \end{cases} \quad (12)$$

Let $\mathbf{E} = \mathbf{M} * \mathbf{A} * \mathbf{D}$. Then LMD operation can be expressed as

$$LMD(\mathbf{I}) = \mathbf{EI} \quad (13)$$

Note that we compute all the operators using the intermediate results at each iteration.

IV. PROPOSED DEBLURRING MODEL

In Section III-B, we have proved that minimizing the term $\|8 - LMD(\cdot)\|_1$ favors clear image rather than blurred image. Introducing this constraint to the conventional deblurring framework, the energy function can be written as

$$\min_{I,k} \|I \otimes k - B\|_2^2 + \mu_1 \|8 - LMD(I)\|_1 + \mu_2 \|\nabla I\|_0 + \mu_3 \|k\|_2^2 \quad (14)$$

where μ_1, μ_2, μ_3 are the positive trade-off parameters. The first term in (14) is the data fidelity term aiming to enforce the similarity between clear output and the blurred input. The second term serves to retain salient edges while removing tiny details. The third regularization term insures the sparsity of the *LMD*. The fourth term keeps the smoothness of the blur kernel.

The flowchart shown in Fig. 3 demonstrates the framework of our proposed model. To solve the latent image and the blur kernel alternately, the energy function Eq. (14) is equivalent to the following two equations:

$$\min_I \|I \otimes k - B\|_2^2 + \mu_1 \|8 - LMD(I)\|_1 + \mu_2 \|\nabla I\|_0 \quad (15)$$
$$\min_k \|I \otimes k - B\|_2^2 + \mu_3 \|k\|_2^2 \quad (16)$$

A. ESTIMATING THE LATENT IMAGE

Considering (15) is a convex optimization problem, we apply the half-quadratic splitting strategy [16] to solve it. Adding the auxiliary variables $f \rightarrow 8 - LMD(I)$, $g \rightarrow \nabla I$, the objective function equals to

$$\min_{I,f,g} \|I \otimes k - B\|_2^2 + \omega_1 \|8 - LMD(I) - f\|_2^2 + \omega_2 \|\nabla I - g\|_2^2 + \mu_1 \|f\|_1 + \mu_2 \|g\|_0 \quad (17)$$

where ω_1 and ω_2 are two penalty parameters. Update I, f, and g alternatively by (18), (19), and (20),

$$\min_{\mathbf{I}} \|\mathbf{KI} - \mathbf{B}\|_2^2 + \omega_1 \|8 - \mathbf{EI} - \mathbf{f}\|_2^2 + \omega_2 \|\nabla \mathbf{I} - \mathbf{g}\|_2^2 \quad (18)$$
$$\min_{\mathbf{f}} \omega_1 \|8 - \mathbf{EI} - \mathbf{f}\|_2^2 + \mu_1 \|\mathbf{f}\|_1 \quad (19)$$
$$\min_{\mathbf{g}} \omega_2 \|\nabla \mathbf{I} - \mathbf{g}\|_2^2 + \mu_2 \|\mathbf{g}\|_0 \quad (20)$$

where $\mathbf{K}$ is the Toeplitz matrix of kernel k, and $\mathbf{B}$, $\mathbf{f}$, and $\mathbf{g}$ are vector forms of B, f,and g, respectively. In the second term of (18), auxiliary variable $\mathbf{h}$ is introduced for $\mathbf{I}$ to ensure both speed and accuracy [46]. Equation. (18) can be written as

$$\min_{\mathbf{I},\mathbf{h}} \|\mathbf{KI} - \mathbf{B}\|_2^2 + \omega_1 \|8 - \mathbf{Eh} - \mathbf{f}\|_2^2 + \omega_2 \|\nabla \mathbf{I} - \mathbf{g}\|_2^2 + \omega_3 \|\mathbf{I} - \mathbf{h}\|_2^2 \quad (21)$$

where ω_3 is a new parameter. Update $\mathbf{I}$ and $\mathbf{h}$ alternatively by (22) and (23),

$$\min_{\mathbf{I}} \|\mathbf{K}\mathbf{I} - \mathbf{B}\|_2^2 + \omega_2 \|\nabla\mathbf{I} - \mathbf{g}\|_2^2 + \omega_3 \|\mathbf{I} - \mathbf{h}\|_2^2 \quad (22)$$

$$\min_{\mathbf{h}} \omega_1 \|8 - \mathbf{E}\mathbf{h} - \mathbf{f}\|_2^2 + \omega_3 \|\mathbf{I} - \mathbf{h}\|_2^2 \quad (23)$$

The optimal solutions of $\mathbf{I}$ and $\mathbf{h}$ are obtained with FFT method directly [22], [26]. Taking the derivative of the variables, then setting them to zeroes, we can easily obtain the optimal solution,

$$\mathbf{I} = \mathcal{F}^{-1}\left(\frac{\overline{\mathcal{F}(\mathbf{K})}\mathcal{F}(\mathbf{B}) + \omega_2\overline{\mathcal{F}(\nabla)}\mathcal{F}(\mathbf{g}) + \omega_3\mathcal{F}(\mathbf{h})}{\overline{\mathcal{F}(\mathbf{K})}\mathcal{F}(\mathbf{K}) + \omega_2\overline{\mathcal{F}(\nabla)}\mathcal{F}(\nabla) + \omega_3}\right) \quad (24)$$

$$\mathbf{h} = \frac{\omega_1\mathbf{E}^T(8 - \mathbf{f}) + \omega_3\mathbf{I}}{\omega_1\mathbf{E}^T\mathbf{E} + \omega_3} \quad (25)$$

where $\mathcal{F}(\cdot)$ indicates FFT, $\mathcal{F}^{-1}(\cdot)$ denotes inverse FFT, and $\overline{\mathcal{F}(\cdot)}$ represents conjugate FFT. Equation. (19) involves L_1-norm term, we calculate the solution of $\mathbf{f}$ on the basis of [6], [7]

$$\mathbf{f} = sign(8 - \mathbf{E}\mathbf{I}) \cdot \max\left(|8 - \mathbf{E}\mathbf{I}| - \frac{\mu_1}{2\omega_1}, 0\right) \quad (26)$$

Equation. (20) contains L_0-norm term [16], the answer of $\mathbf{g}$ is as follows:

$$\mathbf{g} = \begin{cases} \nabla\mathbf{I}, & |\nabla\mathbf{I}|^2 \geq \dfrac{\mu_2}{\omega_2} \\ 0, & otherwise \end{cases} \quad (27)$$

The core processes of the intermediate underlying image restoration are shown in Algorithm1. Similarly to algorithms [46], the sub-problem $\mathbf{h}$ is placed on the inner loop to accelerate the computation.

Algorithm 1 Intermediate Latent Image Restoration

Input: Blurred image B and blur kernel k.
$I \leftarrow B$, $\omega_1 \leftarrow \omega_{1,0}$
while $\omega_1 < \omega_{1,\max}$ **do**
  Slove $\mathbf{E}$ using (13).
  Slove f using (26).
  $\omega_2 \leftarrow \omega_{2,0}$
  while $\omega_2 < \omega_{2,\max}$ **do**
    Slove g using (27).
    $\omega_3 \leftarrow \omega_{3,0}$
    while $\omega_3 < \omega_{3,\max}$ **do**
      Slove h using (25).
      Slove I using (24).
      $\omega_3 \leftarrow 2\omega_3$
    end while
    $\omega_2 \leftarrow 2\omega_2$
  end while
  $\omega_1 \leftarrow 2\omega_1$
end while
Output: Blur kernel k,intermediate latent image I.

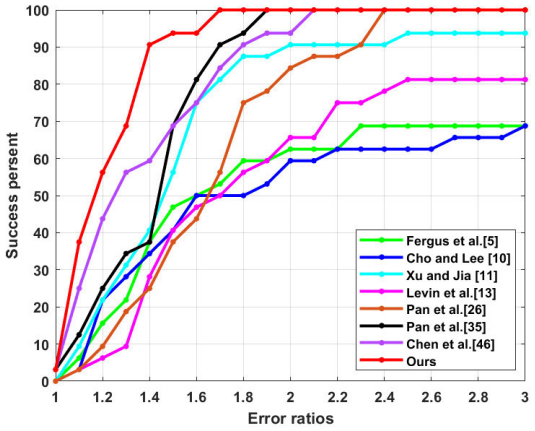

FIGURE 4. Quantitative evaluations on the benchmark dataset [9].

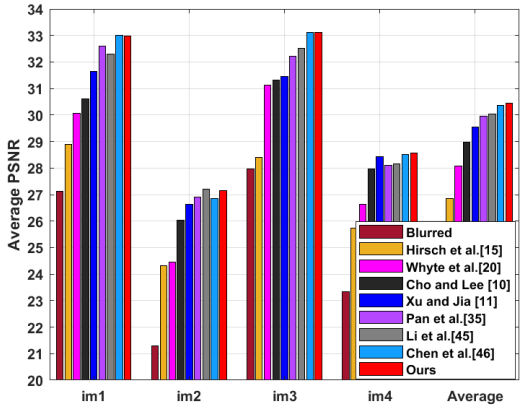

FIGURE 5. Performance comparison on dataset [19].

B. ESTIMATING THE BLUR KERNEL

After the underlying true scene I is estimated, the kernel estimation in Eq.(16) becomes a least-squares minimization problem. The blur kernel restoration method using gradients is more precise than that based on pixel intensity [10].Thus, the blur kernel can be solved in the following manner:

$$\min_k \|\nabla I \otimes k - \nabla B\|^2 + \mu_3 \|k\|^2 \quad (28)$$

The blur kernel k in (28) can be computed using FFT,

$$k = \mathcal{F}^{-1}\left(\frac{\overline{\mathcal{F}(\nabla I)}\mathcal{F}(\nabla B)}{\overline{\mathcal{F}(\nabla I)}\mathcal{F}(\nabla I) + \mu_3}\right) \quad (29)$$

Refer to [13], [22], [26], a multi-scale method is adopted to solve blur kernel [10]. Once the blur kernel k is obtained, we set its negative elements to zero and normalize it. Algorithm 2 displays the key processes of the blur kernel calculation.

V. EXPERIMENTAL RESULTS

In the following part, we conduct experiments on both the synthesized image datasets [9], [19], [26], [34] and real image datasets [34]. The performance evaluation standards such as error ratio [9], peak-signal-to-noise ratio (PSNR) [21], structural similarity (SSIM) [47], and kernel

FIGURE 6. Visual comparisons on a significant blur example from the dataset [19]. (a) Blurred image, (b) Whyte *et al.* [20], (c) Pan *et al.* [35], (d) Chen *et al.* [46], (e) Ours.

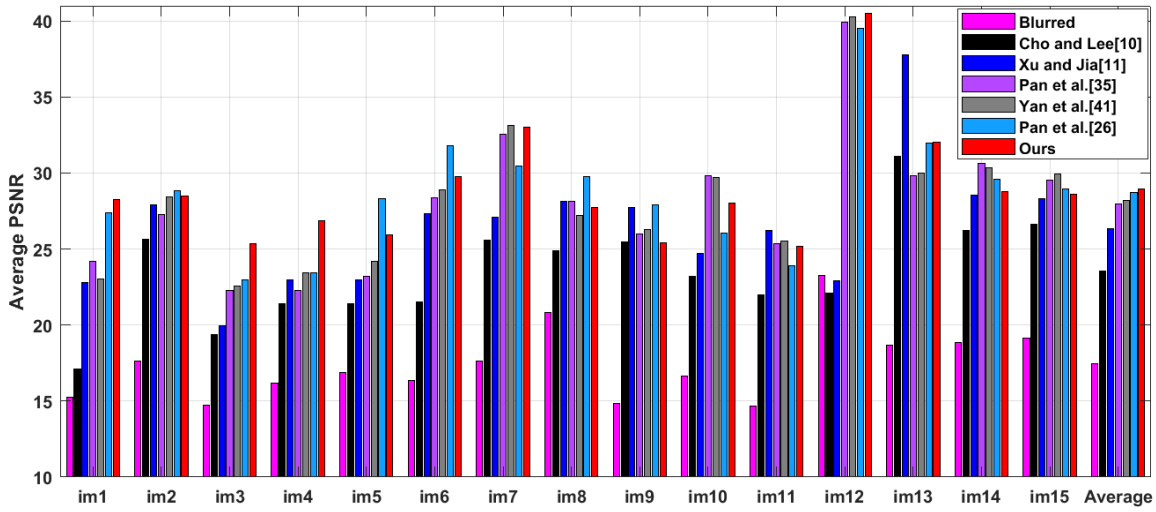

FIGURE 7. Assessment results on the text image dataset [26].

Algorithm 2 Blurred Kernel Estimation Algorithm

Input: Blurred image B.
Initialize k with results from the coarser level.
for $m = 1 : 5$ **do**
  Slove I using Algorithm 1.
  Slove k using (16).
end for
Out put: Blur kernel k and intermediate latent result I.

similarity are utilized to assess the proposed algorithm and other advanced methods.

In all experiments, we use fixed parameters: $\mu_1 = \mu_2 = 0.004$, $\mu_3 = 2$. The size of the *LMD* patch is 35×35. Note that we use the proposed algorithm to obtain the blur kernel, and then make use of a suitable non-blind deblurring method [1], [12], [26]–[28] to recover the last clean image. If not specifically mentioned, the algorithm [26] is utilized to estimate the last clear image. The results of other methods come from two sources. The first is provided by the authors. The second is obtained by running the experiment using the code provided by the author.

A. RESULTS ON SYNTHESIZED IMAGE DATASETS

1) LEVIN'S DATASET

We first compare the presented model with seven other methods [5], [10], [11], [13], [26], [35], [46] on the dataset [9].

TABLE 1. Comparison results on Levin's dataset [9].

	error ratio	PSNR	SSIM
Ground truth	1.0000	32.7201	0.9292
Fergus et al. [5]	11.1109	28.4332	0.8464
Cho and Lee [10]	2.6173	29.6478	0.8821
Xu and Jia [11]	2.1654	30.7015	0.8976
Levin et al. [13]	2.1503	30.0501	0.8956
Pan et al. [26]	1.6442	31.3015	0.9057
Pan et al. [35]	1.3884	31.8711	0.9136
Chen et al. [46]	1.3603	31.6563	0.9123
Ours	**1.2062**	**31.9735**	**0.9172**

Levin's dataset contains four clean scenes and eight kernels. The proposed algorithm performs best in terms of cumulative error ratio, as shown in Fig. 4. When the error ratio is 1.7, our method has a 100% success rate. Chen *et al.*'s method [46] has a 100% success at error-ratio 2.1. Pan *et al.*'s method [35] has a 100% success at error-ratio 1.9. Furthermore, we use the mean error-ratio, mean PSNR, and mean SSIM of the above methods for quantitative comparison. Table 1 shows that the presented algorithm obtains the minimum mean error-ratio, the maximum mean PSNR, and the maximum mean SSIM.

2) KOHLER'S DATASET

Next, we verify the proposed algorithm on dataset [19], which includes 4 clear images and 12 camera motion. The PSNR

TABLE 2. The average PSNR values on the dataset [26].

	Blurred	[10]	[11]	[35]	[41]	[26]	Ours
PSNR(dB)	17.45	23.56	26.36	27.95	28.21	28.73	**28.99**
SSIM	0.53	0.65	0.63	0.79	0.83	0.88	**0.89**

TABLE 3. The average PSNR values on the low-illumination image dataset [26].

	Blurred	[27]	[26]	[35]	[41]	Ours
PSNR(dB)	22.07	23.09	23.84	23.80	23.71	**24.18**
SSIM	0.58	0.66	0.73	0.73	0.72	**0.75**

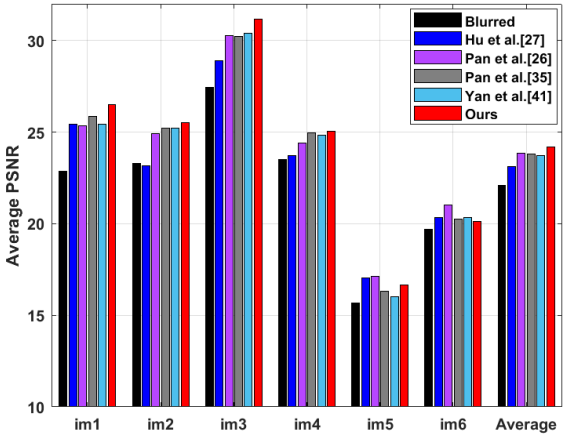

FIGURE 8. Results on the low-illumination image dataset [26].

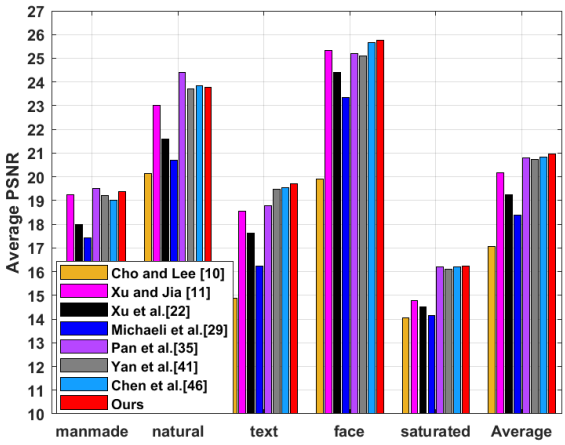

FIGURE 9. Results on Lai et al's dataset [34].

value is calculated by comparing each of the estimated images with 199 original clear images and choosing the best result. From the results in Fig. 5, the presented algorithms obtains the highest total average PSNR value (30.45dB) among state-of-the-art methods [15], [20], [10], [11], [35], [45], [46]. Fig. 6 shows the deblurred results on a significant blur example from this dataset. It is obvious that the proposed generates a clearer result and contains less ringing artifacts than methods [20], [35], [46].

3) TEXT IMAGE DATASET

Moreover, we carry out experiments on Pan's text image datasets [26]. This dataset is constituted of 15 clean document images and 8 kernels from [9]. As one can see from Fig. 7, our approach achieves the highest average PSNR value, outperforms both the advanced methods [10], [11], [35], [41] as well as a specially designed method for text images [26]. The average PSNR and SSIM values of the above methods are demonstrated in Table 2.

4) LOW-ILLUMINATION IMAGE DATASET

We further evaluate our method on Pan's low-light image dataset which involves 6 sharp scenes with 8 blur kernels from [9]. For the sake of fairness, we utilize the identical non-blind deblurring method from [27]. From Fig. 8, our method performs favorably against generic deblurring methods [26], [35], [41] as well as the method tailored to ill-illumination [27]. We list the average PSNR values in Table 3.

5) LAI ET AL'S DATASET

Finally, we examine our method on a synthetic dataset [34]. The dataset includes 25 true scenes and 4 large-scale blur kernels. The 25 clear images are divided into five kinds, including 5 manmade images, 5 natural images, 5 text images, 5 face images, and 5 saturated images. For a fair comparison, the non-blind deblurring method [27] is used to the blurred saturated images and the non-blind deblurring method [26] is applied to the other kinds. From the results in Fig. 9, our approach outperforms the advanced deblurring approaches [10], [11], [22], [29], [35], [41], [46] in terms of PSNR. From the visual comparison in Fig. 10, the blur kernel recovered by our method contains fewer noises, and the restored image is sharper.

B. RESULTS ON TEAL IMAGES

In this section, we evaluate our algorithm on ground-truth specific scenarios images. Unlike the benchmark dataset

FIGURE 10. The deblurred results on a face image form the dataset [34]. (a)The blurred image, (b) Cho and Lee [10], (c) Xu and Jia [11], (d) Xu *et al.* [22], (e) Pan *et al.* [35], (f) Yan *et al.* [41], (g) Chen *et al.* [46], (h) Ours.

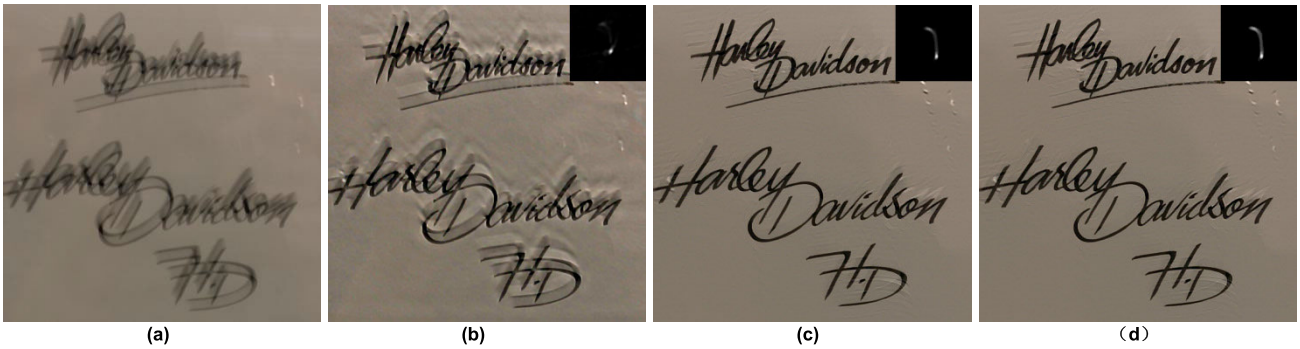

FIGURE 11. The recovered results on a real text image from [34]. (a) Input, (b) Krishnan *et al.* [14], (c) Pan *et al.* [26], (d) Ours.

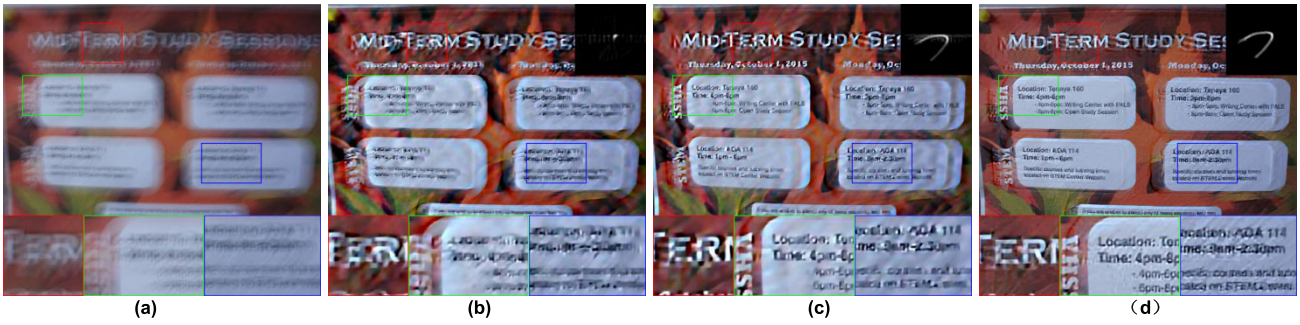

FIGURE 12. The generated results on a real text image with a complex background. (a) The input, (b) Krishnan *et al.* [14], (c) Pan *et al.* [26], (d) Ours.

images, we do not know the true blur kernel of those images. For the sake of fairness, we adopt the same non-blind deconvolution method and set the same blur kernel size. A few examples are shown below to test the effectiveness of our presented method.

Fig. 11 demonstrates the recovered results on a real-world document image. Due to the large-scale blur, the nature image deblurring method [14] fails to yield a clear result. Our approach produces a comparable result to the text image deblurring methods [26]. Fig. 12 illustrates the generated results on a text image with a complex background. Our method generates a better result than state-of-the-art text image deblurring method [26].

We test our method on a real license plate image. Here adopted is the identical non-blind deconvolution algorithm from [27]. As shown in Fig. 13, the result generated by the proposed algorithm has clearer details and fewer artifacts compared with the latest methods [27], [35], [41], [46].

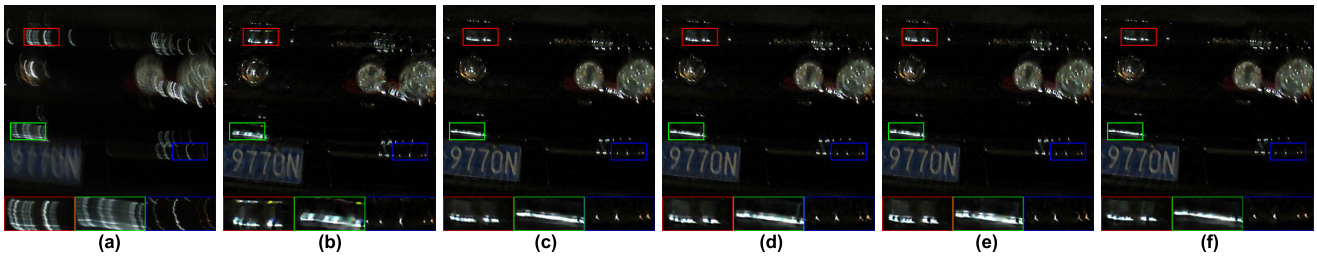

FIGURE 13. Results on a real-world license plate image. (a) Input, (b) Hu *et al.* [27], (c) Pan *et al.* [35], (d) Yan *et al.* [41], (e) Chen *et al.* [46], (f) Ours.

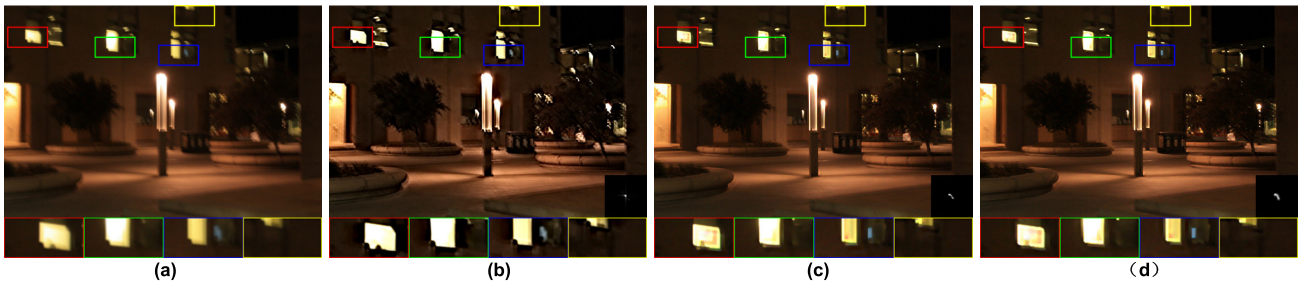

FIGURE 14. Results of a real low-light scene. (a)The input blurred image, (b) Krishnan *et al.* [14], (c) Hu *et al.* [27], (d) Ours.

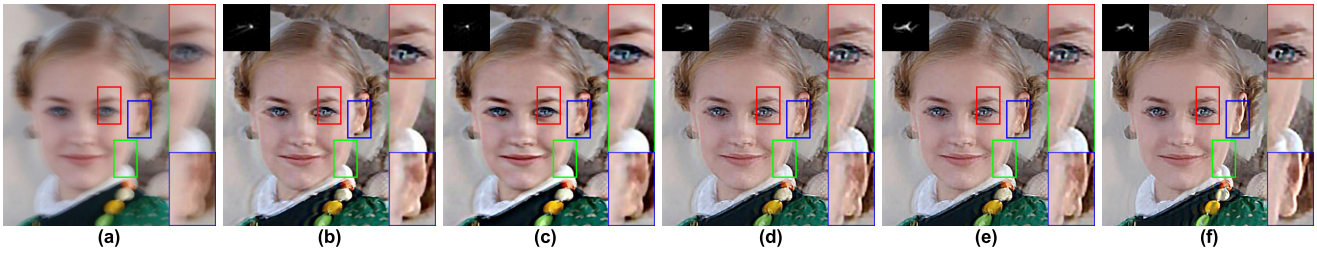

FIGURE 15. Results on a ground-truth face image. (a) Input, (b) Xu and Jia [11], (c) Krishnan *et al.* [14], (d) Yan *et al.* [41], (e) Chen *et al.* [46], (f) Ours.

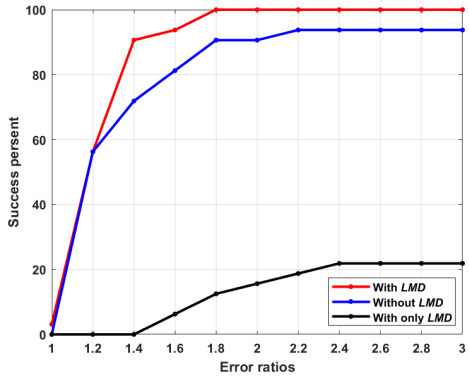

FIGURE 16. The results of three different models on dataset [9].

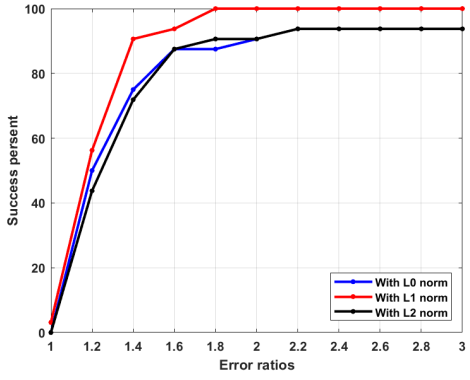

FIGURE 17. Three norm constraints on *LMD* related term.

We demonstrate the ability of our method on low-illumination image deblurring in Fig. 14, where the same non-blind deconvolution method as in [27] is used. Due to the effect of saturated regions, the result of the natural image deblurring method [14] contains obvious ringing artifacts and residual blur. In contrast, our result has fewer residual blur than the advanced low-illumination deblurring methods [27].

We evaluate our method on a real face image. The identical non-blind deconvolution algorithm as in [12] is employed here. As we can see from Fig. 15, the presented algorithm produces a more visually pleasing result than the state-of-art methods [11], [14], [41], [46].

VI. ANALYSIS AND DISCUSSION

In the following part, we show the validity of the proposed regularized prior, compare three different sparsity constraints on the *LMD* involved term, discuss the impact of image patch

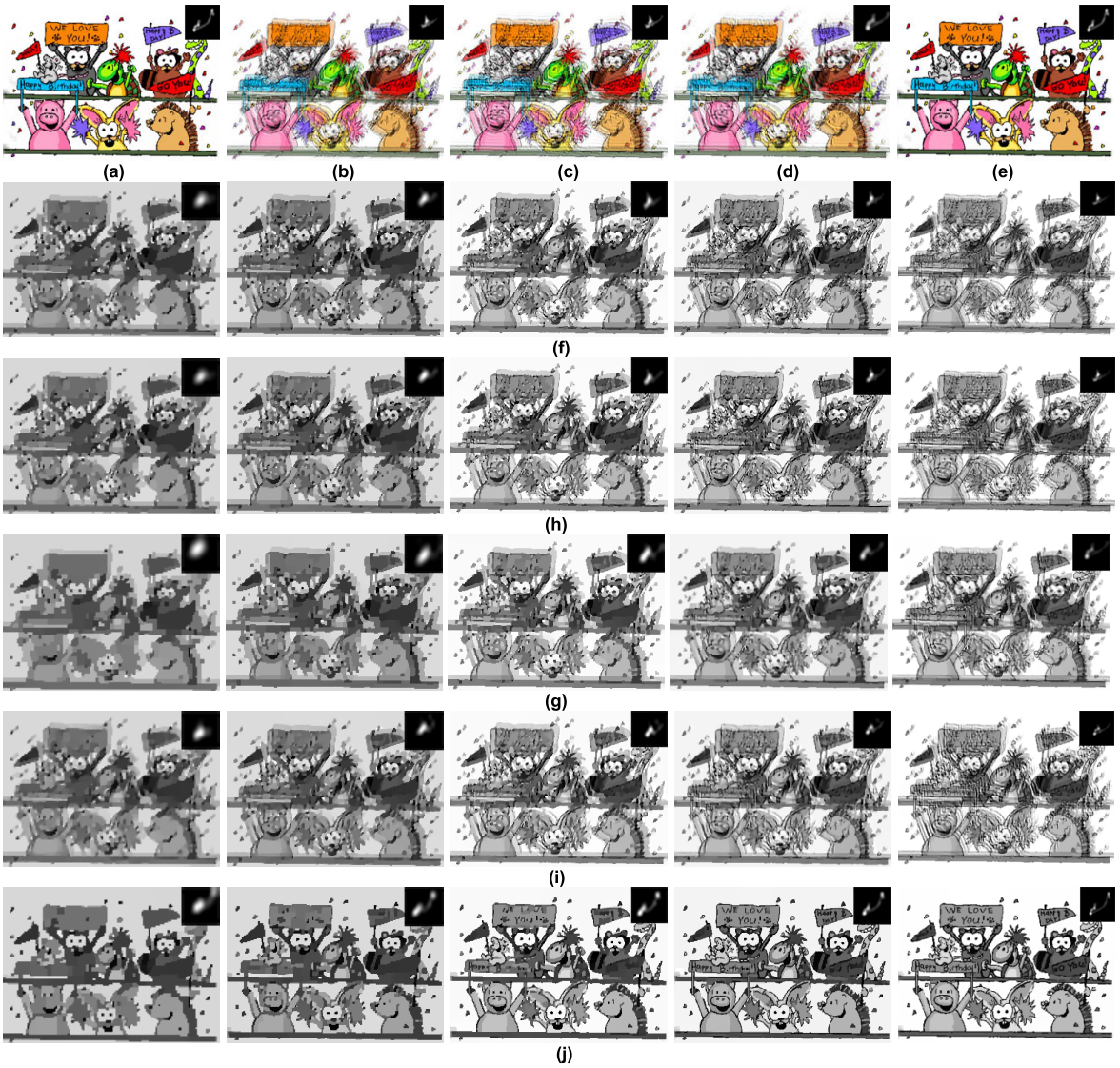

FIGURE 18. The Generated final results and intermediate results of different priors. (a) Input, (b) Pan *et al.* [35], (c) Yan *et al.* [41], (d) Chen *et al.* [46], (e) Ours, (f) Intermediate results of (b), (g) Intermediate results of (c), (h) Intermediate results of d), (i) Intermediate results of our model without *LMD*, (j) Intermediate results of Ours.

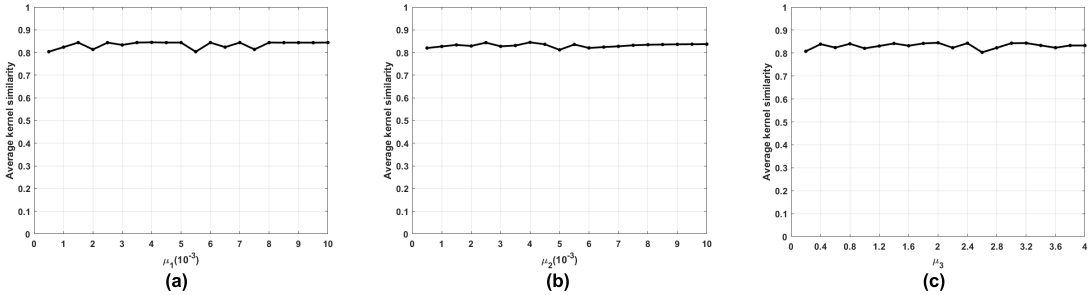

FIGURE 19. Effect of parameters in the goal function. (a) Effect of μ_1, (b) Effect of μ_2, (c) Effect of μ_3.

size for calculating *LMD* and input parameters, and analyze the convergence property and the limitations.

A. EFFECTIVENISS OF LMD PRIOR

To test the effectiveness of the presented prior, we carry out experiments using three different regularization terms on datasets [9] respectively. As shown in Fig. 16, the model with *LMD* prior generates the best results. We compare our prior with the latest intensity-based priors from [35], [41] and gradient-based prior from [46]. Fig. 18 shows the final deblurred results and intermediate results of different priors. Because the true image has fewer extreme pixels,

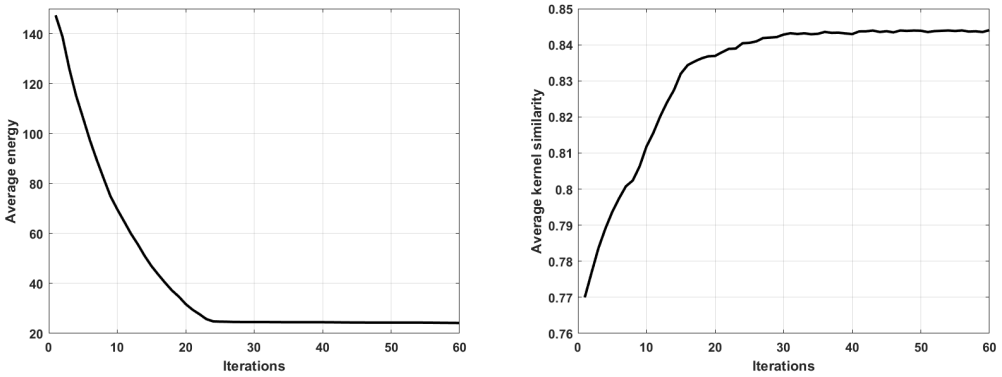

FIGURE 20. The convergence of the presented optimization scheme. (a) The average energy of our objective function at the finest image scale, (b) The average kernel similarity at the finest image scale.

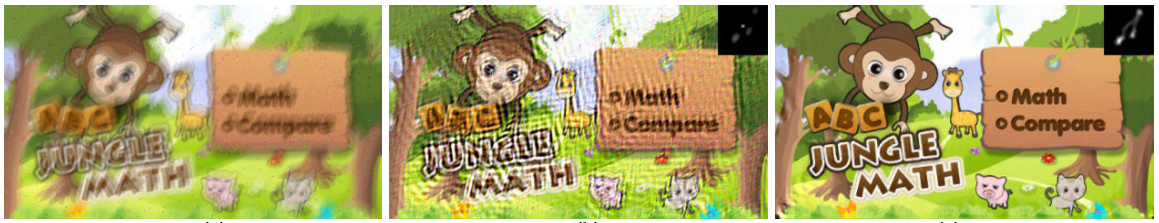

FIGURE 21. The limitation of the *LMD* prior. (a) Input, (b) The result of our method, (c) The result after applying the Median filter.

TABLE 4. Results comparison of different patch sizes on dataset [9].

Patch size	15×15	25×25	35×35	45×45
Avg.PSNR	31.8179	31.7853	**31.9735**	31.7185
SSIM	0.9166	0.9151	**0.9172**	0.9148

methods [35], [41] cannot generate a pleasing result. Due to large-scale blur, the result of the method [46] is still blurred, while the result of our prior is pleasing. Thus we can see that the *LMD* prior of the image is more conducive to restoring the true blur kernel.

B. NORM CONSTRIANS ON THE LMD TERM

In Eq. (14), we use the L_1 norm to constrain the *LMD* involved term. To test the sparsity of the *LMD* prior, we adopt three different norms to perform experiments on the dataset [9]. As can be seen from Fig. 17, the model with L_1 norm generates better results than the other two cases. This means that the sparsity of *LMD* is an intrinsic feature of motion blur which is beneficial to blur kernel estimation.

C. EFFECT OF PATCH SIZE FOR COMPUTING LMD MAP

We discuss the effect of image patch size for computing *LMD* and set four different patch sizes to run experiments on the dataset [9]. We use PSNR and SSIM for performance evaluation. From the results in Table 4, the proposed algorithm is robust to patch size variation.

D. EFFECT OF INPUT PARAMETERS

We analyze the impact of input parameters μ_1, μ_2 and μ_3 in the energy function (14) on the image deblurring performance in terms of kernel similarity. As for parameter μ_1, we fix $\mu_2 = 0.004, \mu_3 = 2$, and vary the values of μ_1 from 0.0005 to 0.001 with the increase step of 0.0005. We perform experiments using Levin's dataset [9], and compare the kernel similarity of these 20 different output images. As can be seen from Fig. 19(a), our method can restore a satisfying blur kernel within a reasonable μ_1. We perform similar experiments for μ_2 and μ_3, Fig. 19(b) and Fig. 19(c) demonstrate that our presented model performs well with a wide range of input parameter settings.

E. CONVERGENCE PROPERTY

In this section, we analyze the convergence of the presented algorithm in terms of energy values and kernel similarity. We perform experiments at the finest image scale using Levin's dataset [9]. We compute the kernel similarity [47] and the energy value (15) at the finest image scale. As illustrated in Fig. 20, our optimization approach converges after 30 iterations.

F. LIMITATIONS

In spite of the robust performance on different datasets, the presented method is prone to failure in processing images with significant non-Gaussian noise. Fig. 21 shows the

TABLE 5. Running time (in second) comparison.

Method	255×255	600×600	800×800
Xu et al. [11]	1.13	3.46	6.59
Krishnan et al. [14]	5.48	45.72	83.94
Pan et al. [35]	135.78	834.95	1592.21
Chen et al. [46]	69.10	423.74	817.25
Ours	75.61	468.16	987.19

generated results of an image with salt and pepper noise. The result of our method is still blurred, the result after applying the Median filter is pleasing. Our future work will focus on joint deblurring and denoising using the LMD.

In addition, computing the *LMD* relevant term involves several nonlinear operations. Therefore, the proposed method is time-consuming. We test the run time on a computer with 16 GB RAM and Intel Core i7-8700 CPU, and summarize the average time in Table 5.

ACKNOWLEDGMENT

The authors would like to thank the reviewers for their helpful comments and suggestions, which greatly improved the quality of the article.

REFERENCES

[1] D. Krishnan and R. Fergus, "Fast image deconvolution using hyper-laplacian priors," in *Proc. Adv. Neural Inf. Process. Syst.*, 2009, pp. 1033–1041.
[2] L. B. Lucy, "An iterative technique for the rectifification of observed distributions," *Astron. J.*, vol. 79, no. 6, pp. 745–754, 1974.
[3] T. F. Chan and C. K. Wong, "Total variation blind deconvolution," *IEEE Trans. Image Process.*, vol. 7, no. 3, pp. 370–375, Mar. 1998.
[4] T. H. Li and K. S. Lii, "A joint estimation approach for two-tone image deblurring by blind deconvolution," in *Proc. ACM Trans. Graph.*, 2002, pp. 847–858.
[5] R. Fergus, B. Singh, A. Hertzmann, S. T. Roweis, and W. T. Freeman, "Removing camera shake from a single photograph," *ACM Trans. Graph.*, vol. 25, no. 3, pp. 787–794, Jul. 2006.
[6] J. Jia, "Single image motion deblurring using transparency," in *Proc. IEEE Conf. Comput. Vis. Pattern Recognit.*, Jun. 2007, pp. 1–8.
[7] Q. Shan, J. Jia, and A. Agarwala, "High-quality motion deblurring from a single image," *ACM Trans. Graph.*, vol. 27, no. 3, p. 73, 2008.
[8] N. Joshi, R. Szeliski, and D. J. Kriegman, "PSF estimation using sharp edge prediction," in *Proc. IEEE Conf. Comput. Vis. Pattern Recognit.*, Jun. 2008, pp. 1–8.
[9] A. Levin, Y. Weiss, F. Durand, and W. T. Freeman, "Understanding and evaluating blind deconvolution algorithms," in *Proc. IEEE Conf. Comput. Vis. Pattern Recognit.*, Jun. 2009, pp. 4003–4011.
[10] S. Cho and S. Lee, "Fast motion deblurring," *ACM Trans. Graph.*, vol. 28, no. 5, p. 145, 2009.
[11] L. Xu and J. Jia, "Two-phase kernel estimation for robust motion deblurring," in *Proc. Eur. Conf. Comput. Vis.*, 2010, pp. 157–170.
[12] S. Cho, J. Wang, and S. Lee, "Handling outliers in non-blind image deconvolution," in *Proc. Int. Conf. Comput. Vis.*, Nov. 2011, pp. 495–502.
[13] A. Levin, Y. Weiss, F. Durand, and W. T. Freeman, "Efficient marginal likelihood optimization in blind deconvolution," in *Proc. CVPR*, Jun. 2011, pp. 2657–2664.
[14] D. Krishnan, T. Tay, and R. Fergus, "Blind deconvolution using a normalized sparsity measure," in *Proc. CVPR*, Jun. 2011, pp. 233–240.
[15] M. Hirsch, C. J. Schuler, S. Harmeling, and B. Scholkopf, "Fast removal of non-uniform camera shake," in *Proc. Int. Conf. Comput. Vis.*, Nov. 2011, pp. 463–470.
[16] L. Xu, L. Cewu, Y. Xu, and J. Jia, "Image smoothing via L_0 gradient minimization," in *Proc. ACM Trans. Graph.*, 2011, pp. 1–12.
[17] H. Lee, C. Jung, and C. Kim, "Blind deblurring of text images using a text-specific hybrid dictionary," *IEEE Trans. Image Process.*, vol. 29, pp. 710–723, 2020.
[18] H. Cho, J. Wang, and S. Lee, "Text image deblurring using text-specific properties," in *Proc. Eur. Conf. Comput. Vis.*, 2012, pp. 524–537.
[19] R. Köhler, M. Hirsch, B. Mohler, B. Schölkopf, and S. Harmeling, "Recording and playback of camera shake: Benchmarking blind deconvolution with a real-world database," in *Proc. Eur. Conf. Comput. Vis.*, 2012, pp. 27–40.
[20] O. Whyte, J. Sivic, A. Zisserman, and J. Ponce, "Non-uniform deblurring for shaken images," *Int. J. Comput. Vis.*, vol. 98, no. 2, pp. 168–186, Jun. 2012.
[21] Z. Wang, A. C. Bovik, H. R. Sheikh, and E. P. Simoncelli, "Image quality assessment: From error visibility to structural similarity," *IEEE Trans. Image Process.*, vol. 13, no. 4, pp. 600–612, Apr. 2004.
[22] L. Xu, S. Zheng, and J. Jia, "Unnatural L_0 sparse representation for natural image deblurring," in *Proc. IEEE Conf. Comput. Vis. Pattern Recognit.*, Jun. 2013, pp. 1107–1114.
[23] L. Sun, S. Cho, J. Wang, and J. Hays, "Edge-based blur kernel estimation using patch priors," in *Proc. IEEE Int. Conf. Comput. Photography (ICCP)*, Apr. 2013, pp. 1–8.
[24] L. Zhong, S. Cho, D. Metaxas, S. Paris, and J. Wang, "Handling noise in single image deblurring using directional filters," in *Proc. IEEE Conf. Comput. Vis. Pattern Recognit.*, Jun. 2013, pp. 612–619.
[25] J. Pan, Z. Hu, and Z. Su, "Deblurring face images with exemplars," in *Proc. Eur. Conf. Comput. Vis.*, Cham, Switzerland, 2014, pp. 47–62.
[26] J. Pan, Z. Hu, and Z. Su, "L_0-regularized intensity and gradient prior for deblurring text images and beyond," *IEEE Trans. Pattern Anal. Mach. Intell.*, vol. 39, no. 2, pp. 342–355, Apr. 2016.
[27] Z. Hu, S. Cho, J. Wang, and M.-H. Yang, "Deblurring low-light images with light streaks," in *Proc. IEEE Conf. Comput. Vis. Pattern Recognit.*, Jun. 2014, pp. 3382–3389.
[28] O. Whyte, J. Sivic, and A. Zisserman, "Deblurring shaken and partially saturated images," in *Proc. IEEE Int. Conf. Comput. Vis. Workshops (ICCV Workshops)*, Nov. 2011, pp. 745–752.
[29] Y. Bahat and M. Irani, "Blind dehazing using internal patch recurrence," in *Proc. IEEE Int. Conf. Comput. Photography (ICCP)*, Cham, Switzerland, May 2016, pp. 783–798.
[30] P. Arbelaez, J. Pont-Tuset, J. Barron, F. Marques, and J. Malik, "Multiscale combinatorial grouping," in *Proc. IEEE Conf. Comput. Vis. Pattern Recognit.*, Jun. 2014, pp. 328–335.
[31] W.-S. Lai, J.-J. Ding, Y.-Y. Lin, and Y.-Y. Chuang, "Blur kernel estimation using normalized color-line priors," in *Proc. IEEE Conf. Comput. Vis. Pattern Recognit. (CVPR)*, Jun. 2015, pp. 64–72.
[32] X. Cao, W. Ren, W. Zuo, X. Guo, and H. Foroosh, "Scene text deblurring using text-specific multiscale dictionaries," *IEEE Trans. Image Process.*, vol. 24, no. 4, pp. 1302–1314, Apr. 2015.
[33] J. Sun, W. Cao, Z. Xu, and J. Ponce, "Learning a convolutional neural network for non-uniform motion blur removal," in *Proc. IEEE Conf. Comput. Vis. Pattern Recognit. (CVPR)*, Boston, MA, USA, Jun. 2015, pp. 769–777.
[34] W.-S. Lai, J.-B. Huang, Z. Hu, N. Ahuja, and M.-H. Yang, "A comparative study for single image blind deblurring," in *Proc. IEEE Conf. Comput. Vis. Pattern Recognit. (CVPR)*, Jun. 2016, pp. 1701–1709.
[35] J. Pan, D. Sun, H. Pfister, and M.-H. Yang, "Blind image deblurring using dark channel prior," *IEEE Trans. Pattern Anal. Mach. Intell.*, vol. 40, no. 10, pp. 1628–1636, 2017.
[36] W. Ren, X. Cao, J. Pan, X. Guo, W. Zuo, and M.-H. Yang, "Image deblurring via enhanced low-rank prior," *IEEE Trans. Image Process.*, vol. 25, no. 7, pp. 3426–3437, Jul. 2016.
[37] Z. Hu, L. Yuan, S. Lin, and M.-H. Yang, "Image deblurring using smartphone inertial sensors," in *Proc. IEEE Conf. Comput. Vis. Pattern Recognit. (CVPR)*, Jun. 2016, pp. 1855–1864.
[38] C. J. Schuler, M. Hirsch, S. Harmeling, and B. Scholkopf, "Learning to deblur," *IEEE Trans. Pattern Anal. Mach. Intell.*, vol. 38, no. 7, pp. 1439–1451, Jul. 2016.
[39] A. Chakrabarti, "A neural approach to blind motion deblurring," in *Proc. Eur. Conf. Comput. Vis.*, 2016, pp. 221–235.
[40] R. Yan and L. Shao, "Blind image blur estimation via deep learning," *IEEE Trans. Image Process.*, vol. 25, no. 4, pp. 1910–1921, Apr. 2016.

[41] Y. Yan, W. Ren, Y. Guo, R. Wang, and X. Cao, "Image deblurring via extreme channels prior," in *Proc. IEEE Conf. Comput. Vis. Pattern Recognit. (CVPR)*, Jul. 2017, pp. 4003–4011.
[42] S. Nah, T. H. Kim, and K. M. Lee, "Deep multi-scale convolutional neural network for dynamic scene deblurring," in *Proc. IEEE Conf. Comput. Vis. Pattern Recognit. (CVPR)*, Jul. 2017, pp. 257–265.
[43] X. Tao, H. Gao, X. Shen, J. Wang, and J. Jia, "Scale-recurrent network for deep image deblurring," in *Proc. IEEE/CVF Conf. Comput. Vis. Pattern Recognit.*, Jun. 2018, pp. 8174–8182.
[44] D. Ren, K. Zhang, Q. Wang, Q. Hu, and W. Zuo, "Neural blind deconvolution using deep priors," in *Proc. IEEE/CVF Conf. Comput. Vis. Pattern Recognit. (CVPR)*, Jun. 2020, pp. 3341–3350.
[45] L. Li, J. Pan, W.-S. Lai, C. Gao, N. Sang, and M.-H. Yang, "Blind image deblurring via deep discriminative priors," *Int. J. Comput. Vis.*, vol. 127, no. 8, pp. 1025–1043, Aug. 2019.
[46] L. Chen, F. Fang, T. Wang, and G. Zhang, "Blind image deblurring with local maximum gradient prior," in *Proc. IEEE/CVF Conf. Comput. Vis. Pattern Recognit. (CVPR)*, Jun. 2019, pp. 1742–1750.
[47] Z. Wang, E. P. Simoncelli, and A. C. Bovik, "Multiscale structural similarity for image quality assessment," in *Proc. 37th Asilomar Conf. Signals, Syst. Comput.*, 2003, pp. 1398–1402.
[48] R. Yasarla, F. Perazzi, and V. M. Patel, "Deblurring face images using uncertainty guided multi-stream semantic networks," *IEEE Trans. Image Process.*, vol. 29, pp. 6251–6263, 2020.

JING LIU received the B.S. degree in mathematics and applied mathematics from the Henan University of Science and Technology, Xinxiang, China, in 2011, and the M.S. degree in computational mathematics from the Hefei University of Technology, Hefei, China, in 2015. She is currently pursuing the Ph.D. degree with the School of Computer and Information, Hefei University of Technology. Her current research interests include image deblurring and enhancement, computer-aided geometric-design, and computer graphics.

JIEQING TAN received the B.S. degree in computational mathematics from Xi'an Jiaotong University, Xi'an, China, in 1984, the M.S. degree in computational mathematics from the Hefei University of Technology, Hefei, China, in 1987, and the Ph.D. degree in computational mathematics from Jilin University, Changchun, China, in 1990. From 1992 to 1993, he held a postdoctoral research position with the Department of Mathematics, Dortmund University, Dortmund, Germany. In 1996, he joined the Department of Mathematics, Hefei University of Technology, as a Professor. In 1999, he was a Visiting Professor with the Department of Mathematics and Computer Science, University of Antwerp, Antwerp, Belgium. From 2005 to 2006, he was a Visiting Professor with the Applied Mathematics Research Center, Delaware State University, Dover, DE, USA. Since 1998, he has been a Doctoral Supervisor. His research interests include nonlinear numerical approximation theory, computer-aided geometric design, computer graphics, image processing, and wavelet analysis.

LEI HE received the B.S. degree in computer science from Central China Normal University, Wuhan, China, in 2002, and the M.S. and Ph.D. degrees in computer application technology from the Hefei University of Technology, Hefei, China, in 2007 and 2015, respectively. In 2002, she joined the Department of Mathematics, Hefei University of Technology, as a Teacher. Since 2015, she has been an Associate Professor and a Master Supervisor. Her current research interests include video/image denoising and video/image super-resolution.

XIANYU GE (Student Member, IEEE) received the B.S. degree in information and computing science from Changchun University, Changchun, China, in 2013, and the M.S. degree in computational mathematics from the Hefei University of Technology, Hefei, China, in 2016, where he is currently pursuing the Ph.D. degree with the School of Computer and Information. His current research interests include image deblurring and enhancement, computer-aided geometric-design, and computer graphics.

DANDAN HU received the B.S. degree in mathematics and applied mathematics from Fuyang Normal University, Fuyang, China, in 2015, and the M.S. degree in computational mathematics from the Hefei University of Technology, Hefei, China, in 2019, where she is currently pursuing the Ph.D. degree with the School of Mathematics. Her current research interests include image deblurring and enhancement, computer-aided geometric-design, and computer graphics.